

# A Detailed Study of Interpretability of Deep Neural Network based Top Taggers

---

**Ayush Khot, Mark S. Neubauer, and Avik Roy<sup>1</sup>**

*Department of Physics & National Center for Supercomputing Applications (NCSA)  
University of Illinois at Urbana-Champaign*

*E-mail:* [akhot2@illinois.edu](mailto:akhot2@illinois.edu), [msn@illinois.edu](mailto:msn@illinois.edu), [avroy@illinois.edu](mailto:avroy@illinois.edu)

**ABSTRACT:** Recent developments in the methods of explainable AI (XAI) methods allow researchers to explore the inner workings of deep neural networks (DNNs), revealing crucial information about input-output relationships and realizing how data connects with machine learning models. In this paper we explore interpretability of DNN models designed to identify jets coming from top quark decay in high energy proton-proton collisions at the Large Hadron Collider (LHC). We review a subset of existing top tagger models and explore different quantitative methods to identify which features play the most important roles in identifying the top jets. We also investigate how and why feature importance varies across different XAI metrics, how feature correlations impact their explainability, and how latent space representations encode information as well as correlate with physically meaningful quantities. Our studies uncover some major pitfalls of existing XAI methods and illustrate how they can be overcome to obtain consistent and meaningful interpretation of these models. We additionally illustrate the activity of hidden layers as Neural Activation Pattern (NAP) diagrams and demonstrate how they can be used to understand how DNNs relay information across the layers and how this understanding can help to make such models significantly simpler by allowing effective model reoptimization and hyperparameter tuning. By incorporating observations from the interpretability studies, we obtain state-of-the-art top tagging performance from augmented implementation of existing networks.

---

<sup>1</sup>Corresponding author.

---

## Contents

<b>1</b>	<b>Introduction</b>	<b>1</b>
<b>2</b>	<b>Review of Top Tagging Dataset and Models</b>	<b>3</b>
<b>3</b>	<b>Interpretability of Machine Learning Models: Tools and Methods</b>	<b>6</b>
<b>4</b>	<b>Model Interpretability for Top Taggers</b>	<b>8</b>
4.1	TopoDNN	9
4.2	MB8S	13
4.3	PFN	17
<b>5</b>	<b>Interpretability Inspires: The Augmented PFN Model</b>	<b>22</b>
<b>6</b>	<b>Conclusion</b>	<b>23</b>
<b>A</b>	<b>Performance of Baseline and variant models</b>	<b>24</b>

---

## 1 Introduction

Machine learning (ML) models are ubiquitous in experimental High Energy Physics (HEP). With an ever increasing volume of data coupled with complex detector phenomenology, these models are useful to find meaningful information from these large datasets. Over time, machine learning models have grown in complexity and simpler regression and classification models have been replaced by intricate and deep neural networks. Owing to their intractably large number of trainable parameters and arbitrarily complex non-linear nature, Deep Neural Networks (DNNs) have often been treated as *black boxes*. It has always been challenging to understand how different input features contribute to the network’s computational process and how the inter-connected neural pathways convey information. In recent years, advances in *explainable* Artificial Intelligence (XAI) [1] have made it possible to build intelligible relationship between an AI model’s inputs, architecture, and predictions [2–4]. While many methods remain model agnostic, a substantial subset of these methods have been developed to infer interpretability of computer vision models where an intuitive reasoning can be extracted from human-annotated datasets to validate XAI techniques. However, in other data structures such as large tabular data or relational data constructs like graphs, use of XAI methods are still quite novel [5, 6]. In recent times, XAI has been successful in learning the underlying physics of a number of problems in high energy detectors [7], including parton showers at the Large Hadron Collider (LHC) [8] and jet reconstruction using particle flow algorithms [9].

One of the major applications of ML in the field of HEP is classification of jets, which is referred to as *jet tagging*. Jets represent hadronic showers observed as a conical spray of particles originating from quarks and gluons produced in the high energy collisions at high energy colliders like the LHC. Identifying jets that originate from decay products of a particle such as the top quark ( $t$ ) and being able to separate them from other jet categories, such as jets originating from the QCD background, is an important challenge in many physics analyses. Traditional top tagging algorithms based on kinematic features of jets and clustering of jet constituents (see Refs. [10–13] for example) have been used in particle phenomenology research as well as by ATLAS and CMS experiments and their predecessors. In Run 1 physics analyses, these top tagging algorithms along with low-complexity statistical models like decision trees took the center stage in dealing with top tagging [14–16]. However, owing to their superior performance, models based on deep neural networks (DNNs) started becoming popular in Run 2 at a higher center-of-mass energy of 13 TeV [17, 18].

For top quarks produced with large momenta, the decay products can be packed close to one another and be reconstructed as a single jet. For such *boosted* jets, top tagging can be particularly challenging and require a better analysis of *jet substructures*, a collection of constituents and their derivative properties that can offer better discrimination between jet classes. DNNs have proven to be useful to exploit the jet substructure properties in performing jet classification. A wide variety of deep learning models have been developed to optimize top tagging [19–32]. A comprehensive review and comparison of many of these models have been given in Ref. [33]. Some of these models have exploited DNN’s capacity to approximate arbitrary non-linear function [34] and their huge success with problems in the field of computer vision, other models have been inspired by the underlying physics information like jet clustering history [22], physical symmetries [23] and physics-inspired feature engineering [27]. These efforts have inspired novel model architectures and feature engineering by creating or augmenting input feature spaces with physically meaningful quantities [27, 35, 36].

The rich history of physics-inspired model development makes the problem of top tagging an excellent playground to better understand the modern XAI tools themselves. This allows us to traverse a rare two-way bridge in exploring the relationship between data and models- our physics knowledge will allow us to better understand the inner workings of modern XAI tools and perfect them while those improved tools would allow us to take a deeper look at the models- paving ways for reoptimizing and improving those models. As it has been pointed out in Ref. [37], such insights into explainability of DNN-based models are important to validate them, to make them reliable and reusable. Additionally, the broader scope of uncertainty quantification in association with ML models relies on developing robust explanations [38] and in the field of HEP for problems like top tagging will require dedicated understanding of how robust as well as interpretable these models are [39].

Yet another remarkable application of interpretability is to understand how the model conveys information and in doing so, which parts of a DNN most actively engage in forward propagation of information. Such studies could be useful to understand and reop-

timize model complexity. Given DNNs have shown remarkable success in jet and event classification, recent work has placed emphasis on developing DNN-enabled FPGAs for trigger-level applications at the LHC [40–42]. As resource consumption and latency of FPGAs directly depend on the size of the network to be implemented, it is definitely easier to embed simpler networks on these devices. Hence, methods that allow interpreting a network’s response patterns as well as provide critical insights about model optimization without compromising its performance can greatly benefit these new budding fields of ML applications, especially for online event selection and jet tagging at current and future high energy colliders.

Application of state-of-the-art explainability techniques for interpreting jet tagger models is receiving more attention recently [36, 43, 44] and has been demonstrated to be successful in identifying feature importance for models like the Interaction Network [45]. In this paper, we study the interpretability of a subset of existing ML-based top tagging models. The models we have chosen use multi-layer perceptrons (MLPs) as underlying neural architecture. Choosing simpler neural architecture allows us to elucidate the applicability and limitations of existing XAI methods and develop new tools to examine them without convoluting these efforts with the complexity of larger models or unorthodox data structures. To compare our results for different models as well as with existing benchmarks in published literature, we use the dataset developed by the authors of Ref. [23] and later used in the top tagger model review in Ref. [33]. The models explored in this paper along with the dataset have been reviewed in section 2. The model hyperparameters explained in this section will constitute the *baseline* model in each category. Variants of each model are studied to better understand their interpretability where the underlying architecture remains the same but model hyperparameters, input features, or data preprocessing might be changed. Section 3 reviews modern XAI methods that we will use in investigating the explainability of top tagger models. In section 4, we analyze the results of applying XAI methods on different top tagger models. Finally, inspired by these models’ inner workings, we achieve state-of-the-art top tagging performance in section 5 by interpretation-inspired augmentation of existing models.

## 2 Review of Top Tagging Dataset and Models

The dataset used in this paper has been used to perform model benchmarking studies in Ref. [33] and publicly available at Ref. [46]. This dataset consists of 1 million top (signal) jets and 1 million QCD (background) jets generated with PYTHIA8 [47] with its default tune at 14 TeV center of mass energy for proton-proton collisions. The detector simulation was performed with DELPHES [48] and jets were reconstructed using the *anti- $k_t$*  algorithm [49] with a jet radius of  $R = 0.8$  using FASTJET [50]. Only jets with transverse momenta within the range of 550 and 650 GeV are considered. For each jet, the dataset contains the four momenta of up to 200 constituents with zero-padded entries for missing constituents. The dataset is split into training, validation, and testing sets with a 6:2:2 split. Some characteristic jet features from a random subsample of the training data are shown in Figure 1.

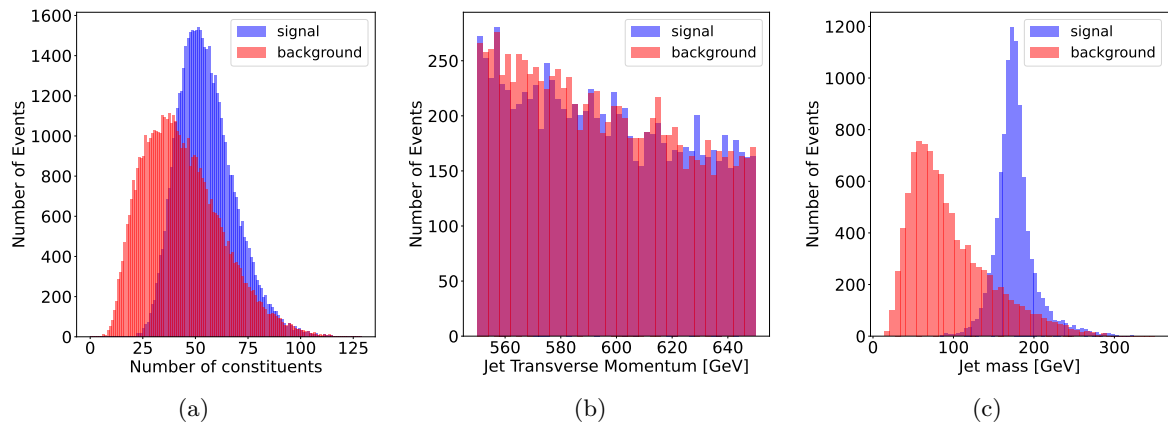


**Figure 1.** Distribution of (a) number of constituent particles, (b) jet transverse momentum ( $p_T$ ), and (c) jet mass for background (QCD) and signal (top) jets

In this paper we consider three different NN-based models for top tagging. Given the tagger distinguishes between two jet classes, minimizing the standard binary cross-entropy (BCE) loss has been used as the training objective for all models. The training is done using the ADAM optimizer with minibatches. All networks showed comparable performance with different batchsizes. The architecture, hyperparameters, and data preprocessing for each of the baseline models is summarized below-

**TopoDNN** [17, 19]: The simplest top tagging model we consider is a fully connected multi-layer perceptron (MLP) trained with transverse momentum ( $p_T$ ), azimuthal angle ( $\phi$ ), and pseudorapidity ( $\eta$ ) of the 30 most energetic particles. Usually referred to as TopoDNN, this model represents a quintessential MLP network. Although TopoDNN is outperformed by many other ML-models for top tagging, its simple architecture allows us to explore different XAI metrics, their limitations, and the best practices to overcome them. Since MLPs are still widely used in HEP for a wide variety of applications, our studies of modern XAI for this model will also illustrate the best practices to interpret the input-output relations for such models.

TopoDNN is trained on preprocessed data where (i) the jet is rotated on the  $\eta - \phi$  plane to have the most energetic component aligned along the central coordinate (0,0), (ii) the second most energetic component falls along the negative- $\phi$  axis, and (iii) all momenta are scaled with an arbitrarily chosen factor of 1/1700. The transformations (i) and (ii) take advantage of the underlying Lorentz invariance of collider physics and (iii) converts the momenta into unitless quantities and scales them down to a numerical range comparable to those of  $\eta, \phi$  quantities. The baseline model is constructed with 4 hidden layers with 300, 102, 12, and 6 nodes respectively and ReLU activation function. The output layer consists of a single node which is converted by the sigmoid function to represent the probability of the jet being classified as a signal jet.

**Multi-body  $N$ -subjettiness (MBNS)** [20, 21]: Top-tagging with  $N$ -subjettiness variables uses an MLP as the underlying trainable architecture. However, the input to the net-

work is different from the usual kinematic variables. It uses the multi-body  $N$ -subjettiness variables [51], defined as

$$\tau_n^{(\beta)} = \frac{1}{p_{T,J}} \sum_i p_{T,i} \min \{ \Delta R_{1i}^\beta, \Delta R_{2i}^\beta, \dots, \Delta R_{ni}^\beta \} \quad (2.1)$$

where  $p_{T,J}$  and  $p_{T,i}$  represent the transverse momenta of the jet and its  $i$ -th constituent and  $\Delta R_{ki}$  is the distance between the  $k$ -th jet axis and the  $i$ -th particle constituent. The  $n$  jet axes chosen for calculating  $\tau_n^{(\beta)}$  are obtained using the  $k_t$  algorithm [52] with  $E$ -scheme recombination [53]. Figure 2 shows the distribution of some of the  $\tau$  variables for QCD and top jets. The input to MBNS tagger is the set of subjettiness variables

$$\{ \tau_1^{(0.5)}, \tau_1^{(1)}, \tau_1^{(2)}, \tau_2^{(0.5)}, \tau_2^{(1)}, \tau_2^{(2)}, \dots, \tau_{N-2}^{(0.5)}, \tau_{N-2}^{(1)}, \tau_{N-2}^{(2)}, \tau_{N-1}^{(1)}, \tau_{N-1}^{(2)} \} \cup \{ p_{T,J}, m_J \} \quad (2.2)$$

where, besides the subjettiness variables, the jet  $p_T$  and jet mass ( $m_J$ ) variables are used as inputs to provide a kinematic scale for the jet event. However, the latter inputs are scaled by a factor of 1/1000 to mitigate the several orders of magnitude gap between their numerical range and those of the  $\tau$ s. In our work we consider the MB8S model- an

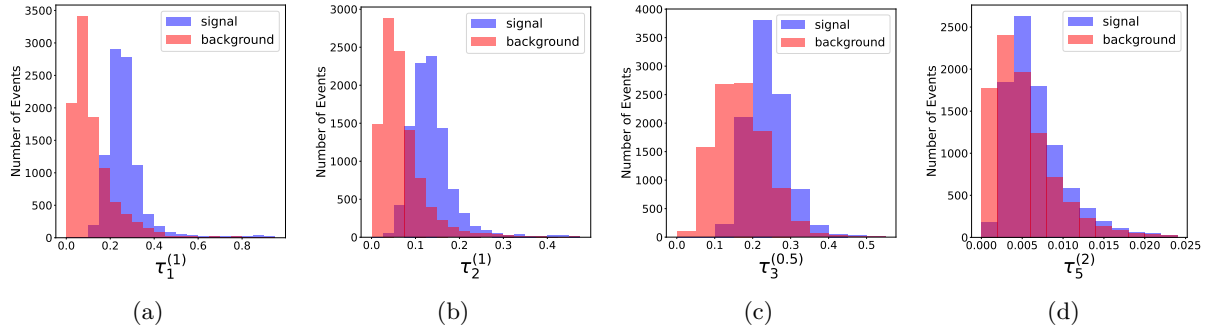


**Figure 2.** Distribution of (a)  $\tau_1^{(1)}$ , (b)  $\tau_2^{(1)}$ , (c)  $\tau_3^{(0.5)}$ , and (d)  $\tau_5^{(2)}$  for background and signal jets

MLP consisting of 4 hidden layers with (200, 200, 50, 50) nodes respectively. The RELU activation function is used for the hidden layers. The output layer consists of 2 nodes transformed by the SOFTMAX function to respectively represent the probabilities of the jet being classified as a background or signal jet.

**Particle Flow Network (PFN)** [24]: PFNs are built as infrared- and colinear- (IRC) safe networks based on the deep set [54] architecture. The deep set architecture inherently makes the network invariant under permutation of particle constituents. The model implements the following relation

$$\text{PFN} = F \left( \sum_{i=0}^{N-1} \Phi(p_i) \right) \quad (2.3)$$

where  $F$  and  $\Phi$  represent non-linear functions implemented as trainable NNs,  $N$  is the number of jet constituents and  $p_i$  is the four momentum of the  $i$ -th jet constituent. We

train the network with the  $p_T, \eta, \phi$  of jet constituents as input. As a part of data pre-processing, we standardized the constituents'  $\eta$  and  $\phi$  by subtracting the jet's  $\eta$  and  $\phi$ . Also, the  $p_T$  values of the jet constituents are scaled by the inverse of sum of constituent  $p_T$ s, i.e.  $1/\sum_i p_{T,i}$ . The  $\Phi$  network is implemented as an MLP with 3 layers of 100, 100, and 256 nodes respectively. Each layer is followed by a RELU activation layer. The output layer of  $\Phi$  represents a 256 dimensional latent space of jet representation. The  $F$  network consists of 3 hidden layers with 100 nodes per layer with RELU activations. The output consists of two nodes transformed by the SOFTMAX operation to represent the probabilities corresponding to each jet class.

### 3 Interpretability of Machine Learning Models: Tools and Methods

While a number of xAI techniques have been developed, how any one these methods actually *explain* an ML model can actually be quite different from the others [55–57]. Often we find the xAI techniques producing diverging explanations, making it challenging to rely on these methods. We investigate a number of these techniques and compare the corresponding results and try to understand what may contribute to their divergence. Here, we summarize the methods that we are going to use to explore the interpretability of top tagger models.

**The  $\Delta$ AUC method:** Identifying feature importance has been an important part of studying classification models [58]. In standard feature selection tasks, a reasonable subset of the features that excels in some model performance metric is chosen. Although it is conceptually different from feature ranking in *post-hoc* model interpretation, many interpretation metrics also rely on identifying feature importance with a simpler surrogate model by trained to minimize a model's performance loss [59]. One of the most useful model analysis tools for binary classification is the Region Operator Characteristic (ROC) curve, and the Area Under the Curve (AUC) serves as a scalar metric for evaluating model performance. ROC-AUC based feature ranking has been widely promoted in ML literature [55, 60, 61]. We adapt those same principles for our model interpretation studies. One straightforward way of evaluating a feature's contribution in making predictions is to investigate the model's performance when a particular feature is masked from the input- by replacing it with a population-wide average value or a zero value, whichever is contextually relevant to the model's relationship with the training dataset.

**Shapely Additive Explanations (SHAP) [62]:** The SHAP scores represent a game theoretic approach in identifying the importance of difference features. For each instance of the dataset, the input features are assigned an additive score that determines to what extent a particular feature contributes to the classifier prediction. An average model prediction is determined by replacing each feature by its population average and then individual features are added back to the model to find their impact on leading the prediction towards the optimal value. For each feature, the SHAP score is determined by evaluating the average contribution of adding the feature over all possible feature subsets defined without that feature. Given that evaluating exact SHAP scores require



iterating over  $2^n$  sets of feature combinations for each data instance with  $n$  features, several simplifying assumptions are made to reduce the computational complexity. In our work, we use the kernel SHAP method- a model agnostic approach to obtain local explanations similar to the LIME framework [63] and obtained by generating random samples around the data point and performing a mean-squared-error-minimizing linear regression over the samples to evaluate the SHAP scores. In order to avoid any overfitting in obtaining the SHAP score, the number of samples in each model were chosen to be at least twice as many as the number of input features

**Layerwise Relevance Propagation (LRP) [64, 65]:** The LRP technique propagates the classification score predicted by the network backwards through the layers of the network and attributes a partial relevance score to each input. The backpropagation of LRP scores in an MLP network is obtained by the following relation-

$$r_j^{(n)} = \sum_k \frac{a_j^{(n)} w_{jk:n}}{\sum_j a_j^{(n)} w_{jk:n}} r_k^{(n+1)} \quad (3.1)$$

where  $a_j^{(n)}$  and  $r_j^{(n)}$  are the activation and relevance scores of the  $j$ -th node in  $n$ -th layer and  $w_{jk:n}$  is the weight that determines the contribution of the  $j$ -th activation in the  $n$ -th layer to the  $k$ -th node in layer  $n + 1$ . The inputs to the network are identified as the 0-th layer and the relevance scores assigned to them are denoted as  $r_j^{(0)}$ . The original LRP method has been developed for simple MLP networks. Variants of this method have been explored to propagate relevance across convolutional neural networks [66] and graph neural networks [67]. While the basic LRP rule in Eqn. 3.1 conserves the total relevance score i.e. the classifier network's output, based on the distribution of weights and activations, relevance scores can become unbounded when  $\sum_k a_j^{(n)} w_{jk:n} \rightarrow 0$ . To overcome this, the LRP rule is modified to treat positive and negative weights asymmetrically. We use the so called LRP- $\gamma$  rule defined as-

$$r_j^{(n)} = \sum_k \frac{a_j^{(n)} (w_{jk:n} + \gamma w_{jk:n}^+)}{\sum_j a_j^{(n)} (w_{jk:n} + \gamma w_{jk:n}^+)} r_k^{(n+1)} \quad (3.2)$$

where  $w^+ = w \cdot \Theta(w)$ ,  $\Theta$  being the Heaviside step function and  $\gamma$  is a regularization parameter. In our representation, we always present the normalized relevance scores so that  $\sum_j r_j^{(0)} = 1$ .

**Neural Activation Pattern (NAP) Diagrams [43, 44]:** While the aforementioned methods help identify the importance of features for a trained NN model, the NAP diagrams visualize the information propagation pathways through the network's architecture. The NAP diagram visualizes the Relative Neural Activation (RNA) score, defined as-

$$\text{RNA}(j, k; \mathcal{S}) = \frac{\sum_{i=1}^N a_{j,k}(s_i)}{\max_j \sum_{i=1}^N a_{j,k}(s_i)} \quad (3.3)$$

where  $\mathcal{S} = \{s_1, s_2 \dots s_N\}$  represents a set of samples over which the RNA score is evaluated. The quantity  $a_{j,k}(s_i)$  is the activation of  $j$ -th neuron in the  $k$ -th layer when the input to



the network is  $s_i$ . When summed over all the samples in the evaluation set  $\mathcal{S}$ , this represents the cumulative neural response of a node, which is normalized with respect to the largest cumulative neural response in the same layer to obtain the RNA score. Hence, in each layer, there will be at least one node with an RNA score of 1. Since the neurons are activated with RELU activation in the models we consider, the RNA score will be strictly non-negative, and  $\leq 1$ . In a qualitative way, we are trying to see which neurons most actively engage to obtain the predictions from our models. Since the MLPs in our models consist of only Dense layers, each layer takes all the activations from the previous layer as inputs. As all nodes within a given layer are subject to the same set of inputs, we can reliably estimate how strongly they perceive and transfer that information to the next layer by looking at their activation values. For the same reason, we normalize the cumulative activation of a node with respect to the largest aggregate in the same layer.

The NAP diagram is obtained by presenting the RNA scores for the different layers of the model as a two dimensional heatmap where along the horizontal axis lies the different activation layers of the network and the vertical axis represents the different nodes in those activation layers. NAP diagrams illustrate the relative activity level of different nodes within each layer and hence can demonstrate the sparsity of the model’s activity.

The methods that we have explored so far adopt widely different approaches to understanding different aspects of a NN. A summary of their properties is given in Table 1. In our analyses, we use models with  $\mathcal{O}(10 - 100)$  inputs, so scalability is not a major bottleneck for application of these methods. On the other hand, although some of these methods allow exploring local explanations, i.e. explanations for individual data samples, we concern our studies with global explanations alone.

	$\Delta\text{AUC}$	SHAP	LRP	RNA/NAP
Scalability in input dimension	✗	✗	✓	✓
Local explanation	✗	✓	✓	✗
Global explanation	✓	✓	✓	✓
Requires Forward Propagation	✓	✓	✓	✓
Requires Backward Propagation	✗	✗	✓	✗

**Table 1.** Comparison of different XAI methods in terms of their implementation heuristics. We consider a method scalable if the complexity of its implementation grows at most by  $\mathcal{O}(n)$ . A local explanation refers to explanation metrics assigned to individual features for a given data point while a global explanation refers to explanation metrics assigned to individual features for the entire dataset.

## 4 Model Interpretability for Top Taggers

Ideally, we expect an XAI metric to correctly identify features that the NN consider most important. Hence, any *post-hoc* feature ranking XAI method should ideally identify the same set of features though their relative rankings can moderately vary. However, there is

no straightforward correlation among XAI methods introduced in the previous section. In order to investigate these methods, we first investigate and validate these methods in the context of simpler TopoDNN and MBNS methods. Then, we use these tools to interpret the PFN model and finally, in the next section, use the insights obtained from these studies to augment the PFN model to obtain state-of-the-art top tagging performance.

#### 4.1 TopoDNN

Since TopoDNN is arguably the simplest NN-based model to perform top tagging, it is perhaps the most ideal model to investigate different aspects of XAI. Given that correlation among features has been demonstrated to be an important aspect of identifying feature rankings in classical machine learning [68] as well as modern XAI methods, we start by examining the pairwise Pearson correlation coefficient for a subset of the input features for background and signal jets in Figure 3. The correlation matrices for both jet categories are mostly sparse except for some large anti-correlations between  $p_{t,0}$ , the transverse momentum of the most energetic jet constituent, and that of some of the low energy constituents. Given the dataset has been generated within a limited jet  $p_T$  range, such anti-correlations are expected- the higher the energy of the most energetic constituent, the lower the energy of the remaining constituents. Given that the numerical range of the  $p_T$  of lower energy constituents is typically much smaller than that of the highest energy constituent, we can expect the impact of their anti-correlations with  $p_{t,0}$  on the NN’s performance to be rather small. We can indeed verify that in Figures 4a–4c where we identify the important features for the TopoDNN model using the  $\Delta\text{AUC}$  (Figure 4a) and SHAP scores (Figures 4b and 4c).

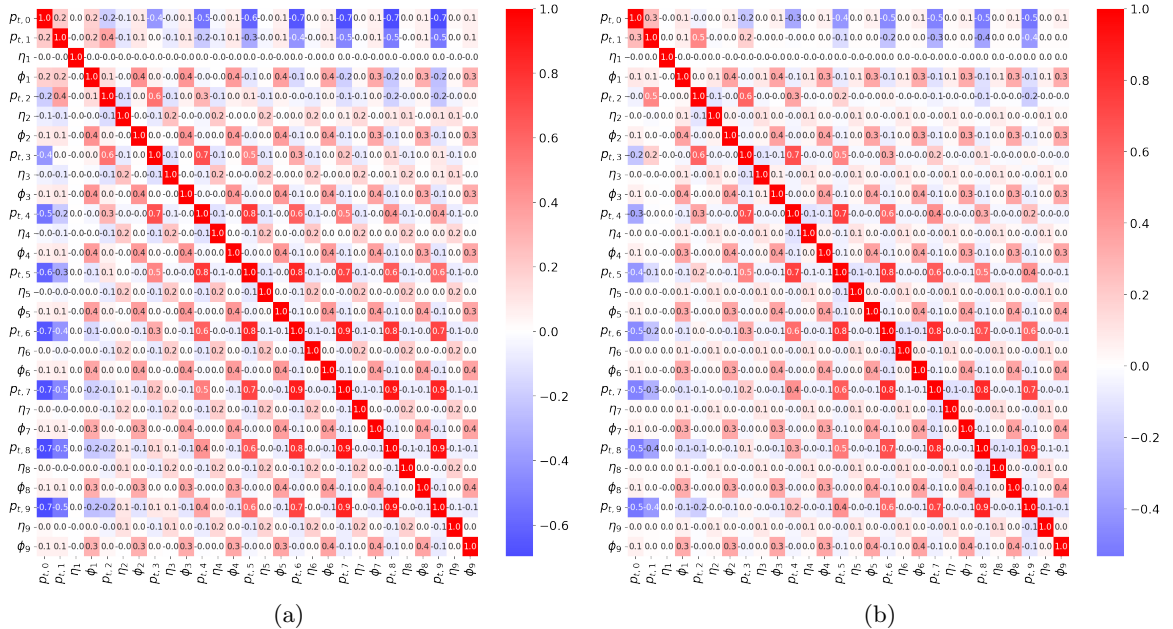


**Figure 3.** Feature correlation matrices for  $p_T$ ,  $\eta$ , and  $\phi$  of the 10 highest energy constituents of (a) background QCD and (b) signal top jets.

The  $\Delta\text{AUC}$  score cannot independently identify the features that contribute to identification of signal and background jets. However, by evaluating the SHAP scores for subsets of the dataset that only contain one kind of jets, one can identify the features that most dominantly contribute to identification of the corresponding jet class. However, as shown in Figures 4b and 4c, there is a significant overlap between the features that are identified as the most important ones for both jet categories. Unlike computer vision models that most deal with image or videos as input data and importance distribution for different images can vary based on which pixels carry the most relevant information, the same feature can contribute equally importantly for different classes in models with tabular data. Why the network treats the same set of variables as important becomes obvious upon inspecting the distribution of some of these preprocessed features as shown in Figures 4d–4g.  $\phi_1, \phi_2, \eta_2$  all show strong classification characteristics, and given these variables are either loosely correlated or almost uncorrelated as shown in Figure 3, they all can independently contribute to the network’s ability to tell apart the different jet classes. On the other hand,  $p_{T,0}$  by itself is a modest discriminator and hence identified as having a modest impact on the model’s performance. This has also been verified by training a variant of the TopoDNN model that excludes the  $p_{T,0}$  variable and as shown in Table A1, performs almost equally as well as the baseline model.

However, we see a stark difference in the distribution of the relevance scores (Figure 5) among different features, obtained from the LRP method, when compared to other feature ranking metrics we have considered so far. Unlike SHAP or  $\Delta\text{AUC}$  scores, a subset of the  $p_T$  variables have the largest relevance scores. While the features mostly highly ranked in the previous two methods show strong discriminating characteristics, some of the highly ranked features from the LRP method show very little discriminating capacity. This difference can be understood from the nature of these ranking methods. Both  $\Delta\text{AUC}$  and SHAP calculate the model’s deviation from the *mean behavior*, i.e. qualitatively, they both represent how much information is obtained from inclusion of the true value of a feature instead of using the population mean as a feature mask. On the other hand, LRP calculates the feature’s cumulative relevance, which additively includes the relevance scores attributed to each feature’s mean behavior. Assuming  $\vec{x} = \{x_i\}$  be a sample jet event taken from the set of events  $X$  and  $\vec{x}_{\setminus k} = \vec{x} \setminus \{x_k\} \cup \{\mathbf{E}(X_k)\}$  be the event set where we mask the  $k$ -th input feature by replacing it with its mean value, the linear order behavior of the NN can be approximated using the Deep Taylor Decomposition formalism [69]–

$$f(\vec{x}) \approx f(\vec{x}_{\setminus k}) + \frac{\partial f}{\partial x_k} (x_k - \bar{x}_k) \quad (4.1)$$

where  $f(\vec{x})$  represents the output of the NN before the final SIGMOID activation. Noting that the relevance scores additively distribute the functional output among the different inputs, i.e.  $f(\vec{x}) = \sum_i r(x_i)$  and  $f(\vec{x}_{\setminus k}) = \sum_{i \neq k} r(x_i) + r(\bar{x}_k)$ , we can rewrite Eqn. 4.1 as,

$$\sum_i r(x_i) \approx \sum_{i \neq k} r(x_i) + r(\bar{x}_k) + \frac{\partial f}{\partial x_k} (x_k - \bar{x}_k) \quad (4.2)$$

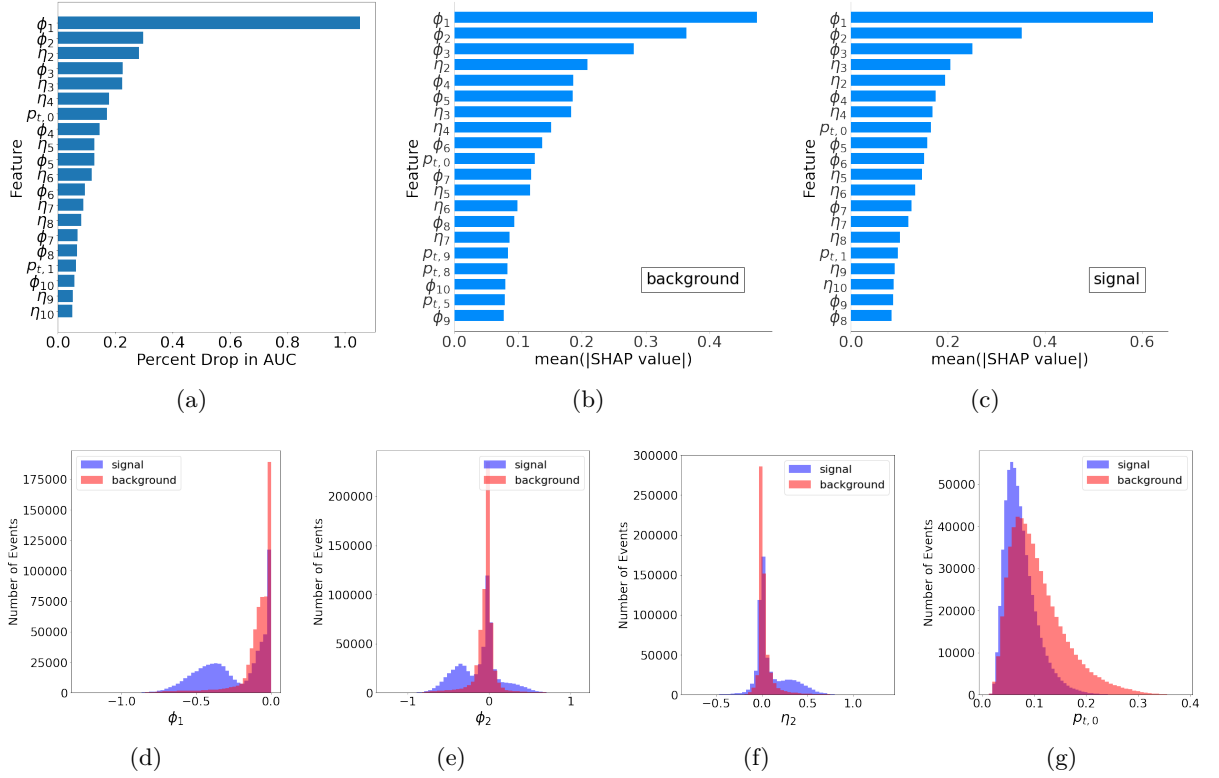


**Figure 4.** Feature rankings obtained from the (a)  $\Delta$ AUC scores, (b) SHAP scores for background QCD, and (c) SHAP scores for signal top jets. Only the 20 highest-ranked features are shown for each jet category. Figures (d), (e), (f), (g) show the distributions of the inputs  $\phi_1$ ,  $\phi_2$ ,  $\eta_2$ , and  $p_{t,0}$  for two jet categories after performing the preprocessing described in Section 2.

We define  $\delta r_k = f(\vec{x}) - f(\vec{x}_{\setminus k}) \approx \frac{\partial f}{\partial x_k} (x_k - \bar{x}_k)$  as the *differential relevance score* attributed to the corresponding feature. When the features are loosely correlated, collecting terms with equivalent indices in Eqn. 4.2 and ignoring higher order effects, we can write  $r(x_k) \approx r(\bar{x}_k) + \delta r_k$  where we denote  $r(\bar{x}_k)$  as the *mean-behavior relevance score*. Figure 6a show the absolute mean behavior relevance scores of different features and the relative size and distribution of the relevance scores are very similar to what we can see in Figure 5. This explains that a large contribution of the LRP scores actually comes from the mean behavior relevances, and has very little to do with the network’s ability to distinguish different jet types. In fact, many of the angular variables that are regarded as highly important by  $\Delta$ AUC and SHAP methods also show large differential relevance, as shown in the distributions of Mean Absolute Differential Relevance (MAD Relevance) scores (normalized with respect to relevance scores from the baseline model) in Figures 6b and 6c.

Now we turn our focus to examine the behavior of the internal architecture of the model with NAP diagrams. As discussed in Section 3, NAP diagrams plot the RNA scores of different nodes of the activation layers within the network. Figure 7 shows the 2D map of RNA scores for QCD and top jets where the RNA scores of the former are plotted as negative values to allow simultaneous visualization. It can be readily understood that the

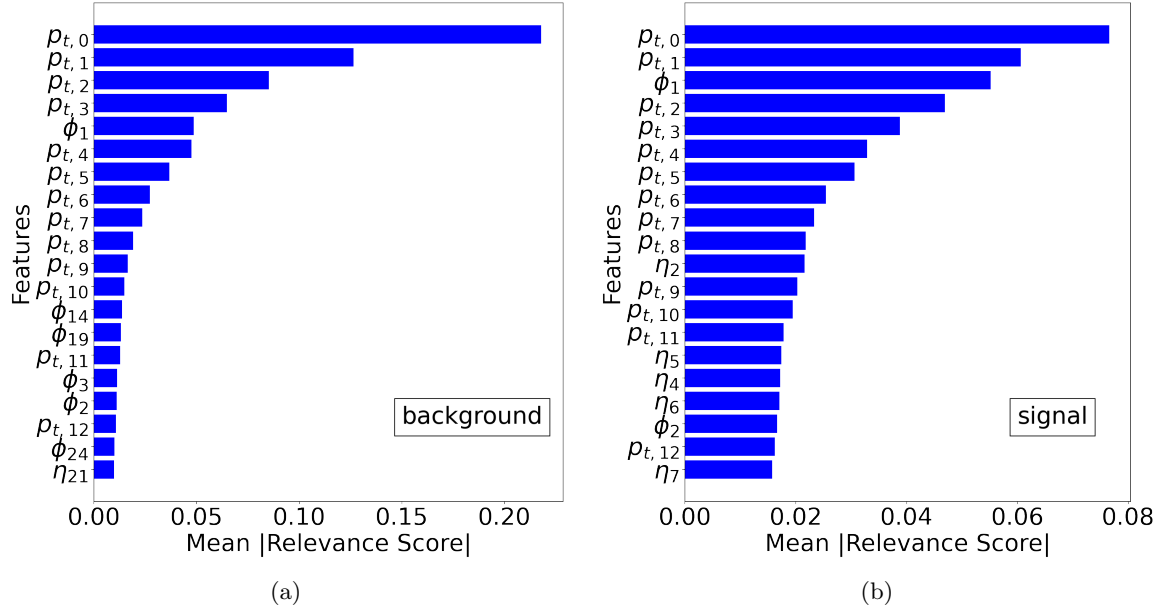


**Figure 5.** Distribution of the relevance scores obtained from LRP for (a) background QCD and (b) signal top jets. Only the 20 highest-ranked features are shown for each jet category.

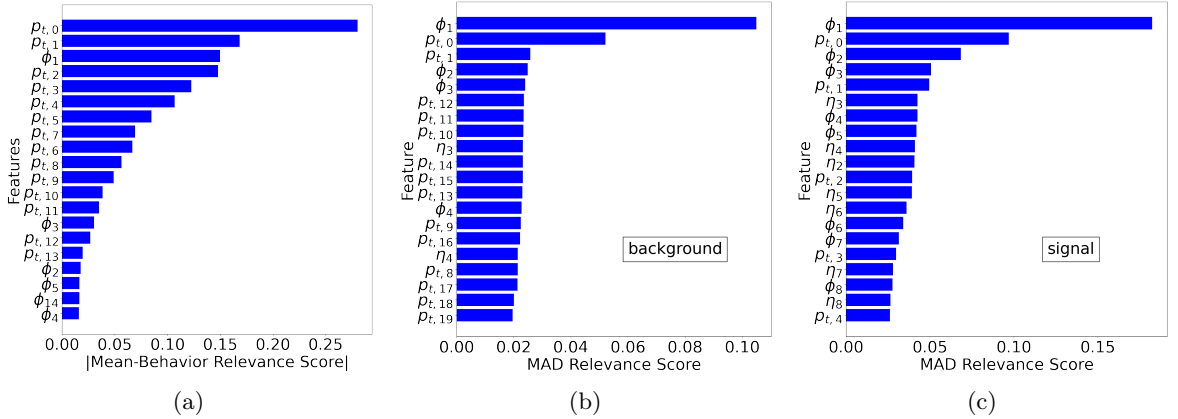


**Figure 6.** Distribution of the (a) absolute mean behavior relevance scores, (b) MAD relevance score for background QCD, and (c) MAD relevance score signal top jets. Only the 20 highest-ranked features are shown for each jet category.

network in Figure 7 is quite *sparse*, i.e. most nodes show relatively smaller activations. We can heuristically quantify *sparsity* of the network by the fractional number of hidden activation nodes with an RNA score less than a given threshold. We arbitrarily choose this threshold to be 0.2 and find that the network’s sparsity measures for background and signal jet categories are 0.86 and 0.76 respectively, giving an overall sparsity measure of 0.70. This implies that about 70% of the nodes show a cumulative activity level of less than 20% compared to that of the most active node in the corresponding layer. We also see in Figure 7 that the most active nodes for different jet categories are almost completely

disentangled by the time information propagates to the third layer. Large sparsity of the network and early disentanglement of jet categories indicate the network’s complexity can be reduced without any noticeable compromise in its performance. To demonstrate this, we have trained variants of the TopoDNN model with lesser complexity by simultaneously reducing the depth and width of the MLP model. As shown in Table A1, these simplified models perform almost equally well while the model complexity is significantly reduced.

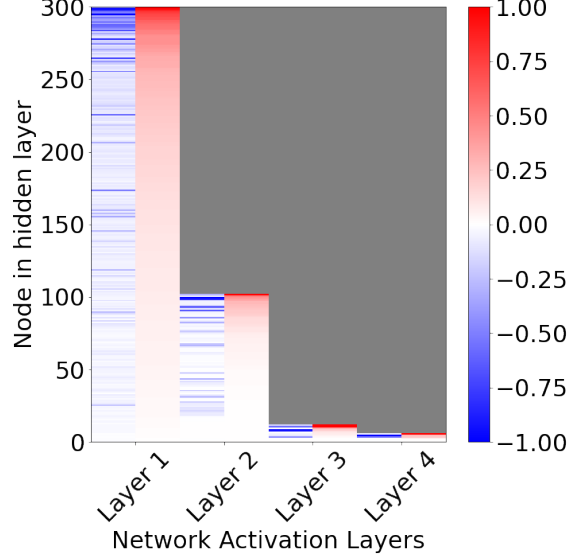


**Figure 7.** NAP diagram for TopoDNN model visualizing a 2D map of RNA score for different nodes of the activation layers. To simultaneously visualize the scores for QCD and top jets, we project the RNA scores of the former as negative values. The nodes in each layer are ordered according to their RNA scores for the top jets.

## 4.2 MB8S

Although the underlying architecture of the MB8S model is an MLP, there is stark difference among the input features. Unlike the input to the TopoDNN model explored in Section 4.1, the inputs to the MB8S model are highly correlated for both jet categories (Figure 8). Such large correlations among features can make it hard to distinguish whether a feature truly conveys independent discriminating characteristics or if a feature is deemed important by a model simply because it is correlated with another feature. Training a NN with correlated feature inputs can contribute to increased model complexity [70], overfitting [71], and obscure its interpretability [72]. The MB8S network has been trained with DROPOUT layers [73] with a dropout rate of 0.2 (0.1) for the first (final) two hidden layers to protect it from the problem of overfitting. With such large correlations among input features, we want to differentiate between two aspects of a feature’s importance- its independent contribution to a network’s decision making process and its deemed importance in a certain instance of a trained model because of its correlations with other models.

Figure 9a shows the distribution of  $\Delta\text{AUC}$  score for the top 10 features. When compared with the SHAP score distributions for background and signal jets in Figures 9b and





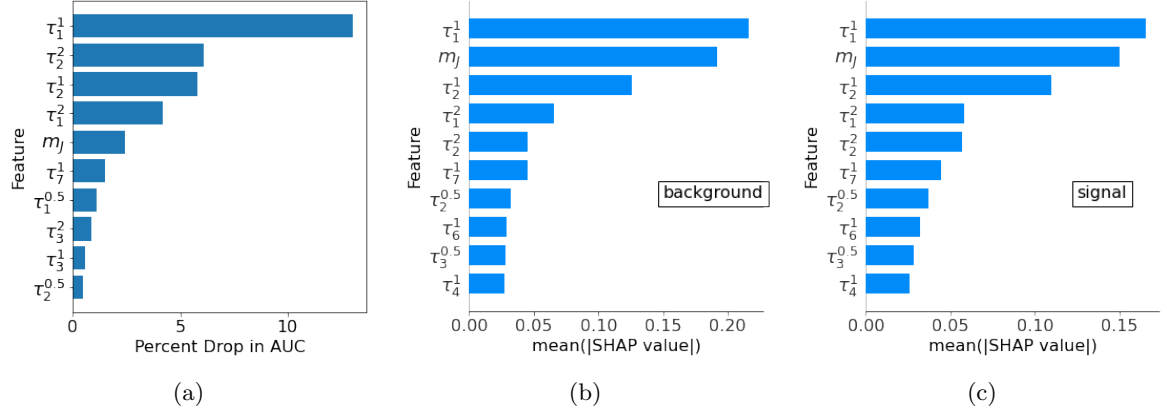


**Figure 9.** Feature rankings obtained from the (a)  $\Delta$ AUC scores, (b) SHAP scores for background QCD, and (c) SHAP scores for signal top jets for the MB8S network. Only the 10 highest-ranked features are shown.

to the baseline MB8S network as shown in Table A1. The feature rankings via  $\Delta$ AUC and SHAP scores for this network also consistently identify  $\tau_1^{(1)}$ ,  $\tau_2^{(1)}$ , and jet mass as the most important features for this classification model. These top ranking features display relatively weaker correlations among themselves (correlation coefficients  $\leq 0.4$ ) and hence, can contribute new information to the classifier’s decision making process. Moreover, since the two networks demonstrate almost equivalent performance, the highly correlated sub-jettiness variables only marginally impact the network’s performance. The relatively high  $\Delta$ AUC score attributed to  $\tau_1^{(2)}$  and  $\tau_2^{(2)}$  in Figure 9a must be an artifact of strong feature correlations. This, however, does not imply that these features are unimportant for the trained network. On the contrary, the large  $\Delta$ AUC scores associated with these variables indicate that the trained MB8S model depends on these correlations for proper inference.

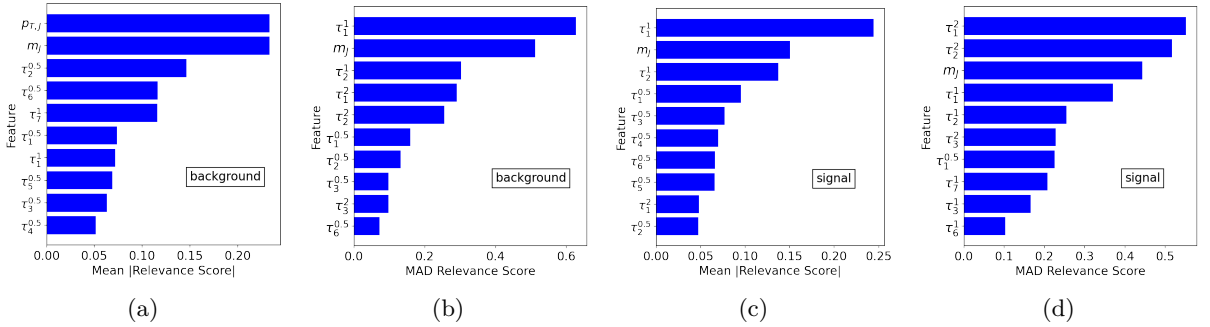


**Figure 10.** Distribution of (a) relevance scores for background QCD, (b) MAD relevance scores for background QCD, (c) relevance scores for signal top jets, and (d) MAD relevance scores for signal top jets for the MB8S network. Only the 10 highest-ranked features are shown for each jet category.

Next we turn our attention to relevance scores attributed to different input features by the LRP method. From our studies of the LRP method for the TopoDNN model, we know

the relevance scores can be an unreliable measure in identifying how important a feature really is. We can see that pattern repeated for the MB8S network too. Figures 10a and 10c show the mean absolute relevance scores attributed to different features for background and signal jets. LRP attributes a large relevance score to  $p_{T,J}$ , the transverse momentum of the jet for the background jets. However, this variable is one of the least expressive features for the network. It has almost no correlation with other features, and has a very similar distribution for both jet types. Hence, assigning this feature a very large relevance score definitely raises some concerns about reliability of the feature ranking obtained from LRP. However, the distribution of MAD relevance scores in Figure 10b gives a more appropriate distribution for feature importances. We note that for the top jets, the relevance distribution identifies  $\tau_1^{(2)}, \tau_2^{(2)}, m_J$  as the most important features.  $\tau_1^{(2)}, \tau_2^{(2)}$  also ranked high in the  $\Delta\text{AUC}$  metric and we have explained how their importance primarily stems from their correlations with other expressive input features to the network.

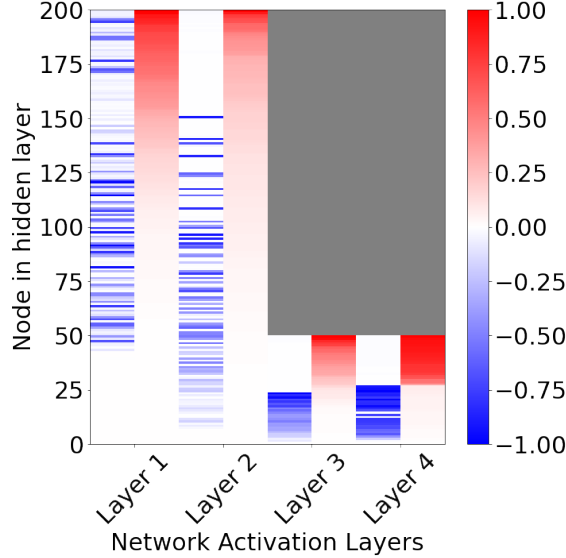


**Figure 11.** NAP diagram for MB8S model visualizing a 2D map of RNA score for different nodes of the activation layers. To simultaneously visualize the scores for QCD and top jets, we project the RNA scores of the former as negative values. The nodes in each layer are ordered according to their RNA scores for the top jets.

To demonstrate how the different hidden activation layers contribute to information propagation for the two jet categories, we show the 2D map of the RNA scores of different nodes in Figure 11. Although the network appears to be relatively sparse for different jet categories, with a sparsity measure of 0.74 and 0.64 for background and signal jets measured with respect to a threshold of 0.2 on RNA scores, different nodes are most strongly activated for signal and jet categories. As a result, the network’s overall sparsity becomes 0.44. However, we can already see that the nodes that are most strongly activated by the two jet categories are almost completely disentangled at Layer 2. This indicates that the network might be simplified by choosing a shallower network and indeed verified

in Table A1 where we see that models trained without the last and the final two layers have almost identical performance metrics.

### 4.3 PFN

While the previously analyzed TopoDNN and MB8S models both employed a single MLP to perform the jet classification, PFN utilizes a deep set topology that linearly combines particle-level neural embeddings to obtain a jet level latent space, which eventually is used to train a second MLP to learn the classification task. Before going into details about interpretability of PFN, we would like to point out that our implementation of PFN obtained significantly better performance benchmark compared to what is reported in Ref. [33] where the different models reported accuracies between 0.89 and 0.93 with ROC-AUC score ranging between 0.955 and 0.985. We obtained an accuracy of 0.977 and an ROC-AUC score of 0.997, which also outperforms the permutation invariant symmetry-guided PELICAN [31], graph-based Interaction Network (IN) [29] and LorentzNet [30] models as well as the transformer-based Particle Transformer (ParT) [32] model. The major difference comes from the model’s inputs. While the PFN model trained in Refs [33] directly used the constituents’ four momenta as input to the, we trained the network with  $p_T, \eta, \phi$  variables of the constituents. The constituent  $\eta$  and  $\phi$  values were standardized according to the prescription in Ref. [24] where  $(\eta_i, \phi_i, p_{T,i}) \rightarrow (\eta_i - \eta_J, \phi_i - \phi_J, \frac{p_{T,i}}{\sum_i p_{T,i}})$ .

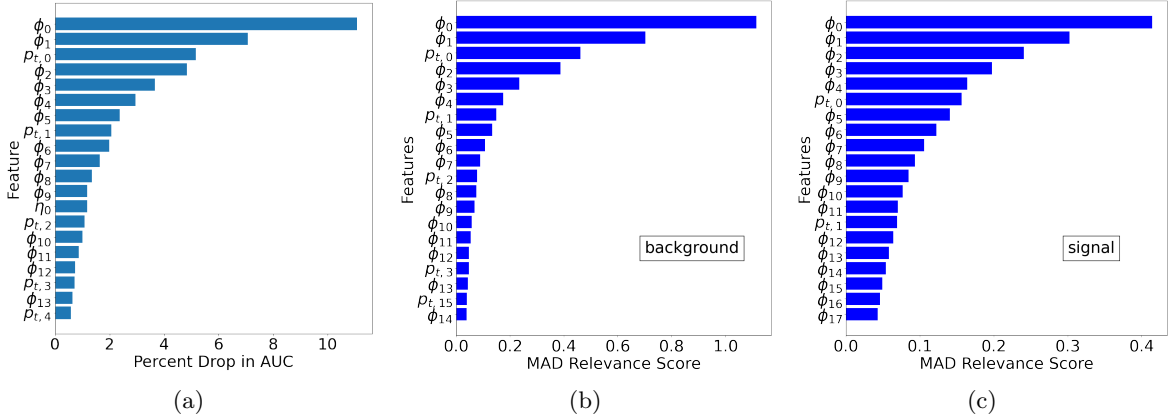


**Figure 12.** Feature rankings obtained from the (a)  $\Delta$ AUC scores, (b) MAD relevance scores for background QCD, and (c) MAD relevance scores for signal top jets for the PFN network. Only the 20 highest-ranked features are shown for each jet category.

We start by examining the feature ranking from the  $\Delta$ AUC and MAD relevance scores in Figure 12. The rankings obtained from both methods show a consistent distribution with the azimuthal distribution of the higher energy constituents being identified as some of the most important features, along with the transverse momenta of the two most energetic constituents. Although the TopoDNN network is also trained on a similar set of input and there is some overlap in the set of important features for these two networks, there are two major differences that prohibit one-to-one comparison between the feature rankings for these variables. Firstly, the input data preprocessing is very different for these two

networks which may result into significant differences on how these variables are treated by the corresponding models. And secondly, particle-level information fed to PFN is directly used to obtain particle-level neural embeddings while they are directly used to perform jet classification for the TopoDNN network. Hence, the importance metric attributed to each component in PFN is indicative of how impactful that constituent is in obtaining the jet level embedding while the relative ranking of the features of a given constituent suggests how important those features are for the network to obtain the constituent level embedding. For instance, the variables  $\phi$  and  $p_T$  for any given constituent outrank the corresponding  $\eta$  which suggests that the  $\Phi$  network assigns more importance to the former in order to obtain its neural embedding.

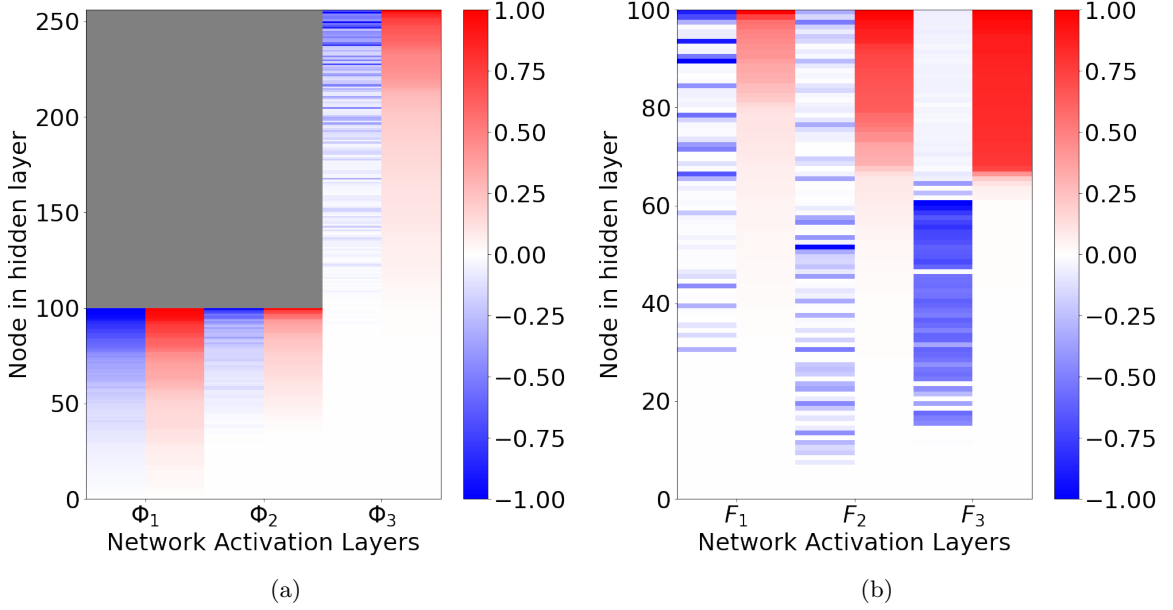


**Figure 13.** NAP diagrams for (a)  $\Phi$  and (b)  $F$  networks for the PFN model. The nodes in each layer are ordered according to their RNA scores for the top jets.

The particle level embeddings obtained by the  $\Phi$  network are summed over to obtain a latent space representation of the jet. Characterization of latent spaces has been a topic of general interest in many areas of machine learning application. For instance, disentangling semantic features of images via latent spaces in Variational AutoEncoders (VAEs) [74] and its variants [75–77] has been widely studied in modern machine learning literature. In the context of collider physics, how latent spaces embed information and can be used as effective candidates for anomaly detection and bump hunting has been studied [24, 29, 78]. The proponents of PFN performed detailed studies showing how the latent space representation forms discernible contours in the  $(\eta, \phi)$  plane of jet image representations. While such studies are useful to divulge geometric features of the latent space configuration, interpreting how they actually contribute to the network’s decision making process, especially for large latent spaces with  $\mathcal{O}(100)$ -dimensions, remains unexplored.

The PFN network is trained to obtain classification scores in two disentangled dimen-

sions in the very last layer of  $F$  network, it is only expected that the information propagation pathways for the different types of jets will show some level of disentanglement within the hidden layers of the networks. This is indeed verified by the NAP diagrams shown in Figure 13. These NAP diagrams reveal some crucial insights. Firstly, we clearly see that the activity level of different nodes in the final layer of the  $\Phi$  network for background and signal jets is very similar. It implies that the network embeds the jet-level information in the same latent subspace. Secondly, the latent space appears to be very sparse and we indeed found that many of the latent space variables are identically zero for all events in both jet categories. We retrained variant networks with latent space dimensions of 128 and 64 and still got comparable performance (Table A1). A third observation is that the  $F$  network effectively learns to disentangle the representation of jet classes by the second hidden layer (Figure 13b). This implies that the network can be simplified by reducing the number of hidden layers. Building on top of these observations, we trained alternate models with modified number of nodes in different hidden layers of the two networks and found that the network’s accuracy is only marginally compromised even with much smaller networks.

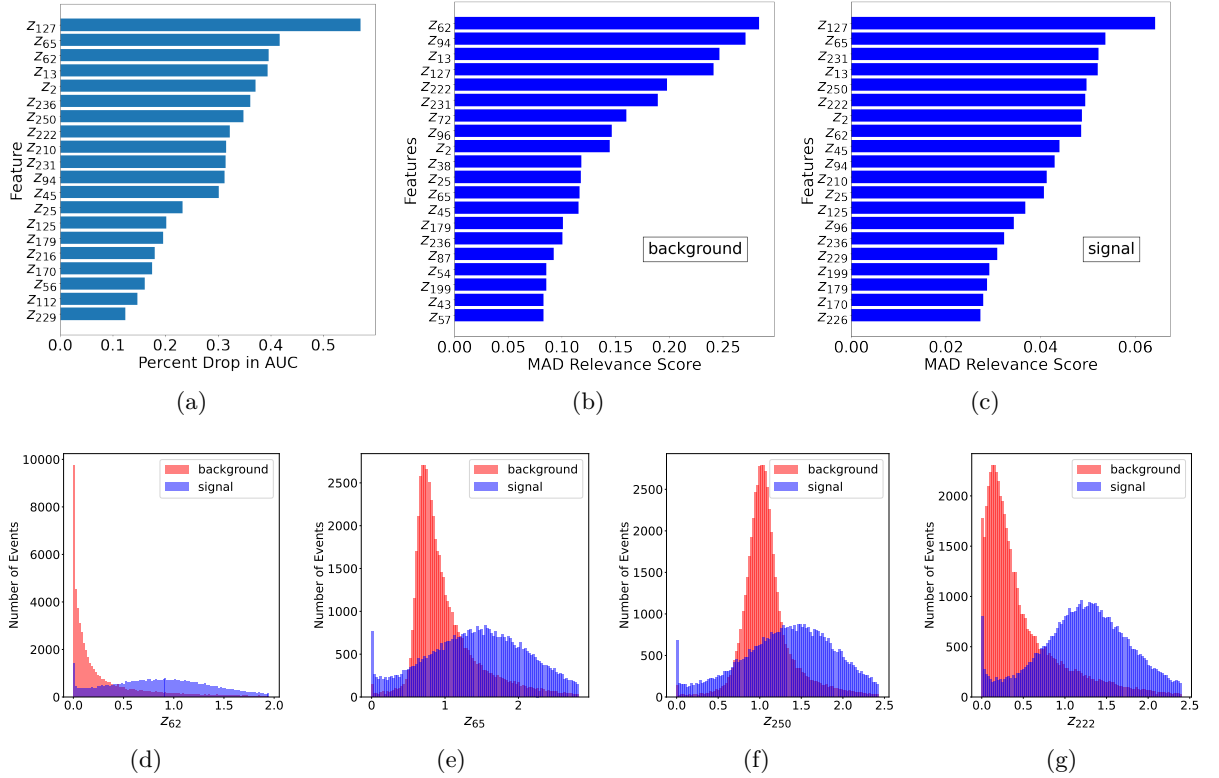


**Figure 14.** Latent space feature rankings obtained from the (a)  $\Delta$ AUC scores, (b) MAD relevance scores for background QCD, and (c) MAD relevance scores for signal top jets. Only the 20 highest-ranked features are shown for each jet category. Figures in the bottom row show the distribution of some of the highest-ranked latent space features for both jet categories.

Given the sparsity of the latent space representation, we expect that only a small sub-

set of these latent features will actually have a strong contribution towards the decision making process of  $F$  in the baseline model. The ranking of different features using the  $\Delta\text{AUC}$  score and MAD relevance scores are shown in Figures 14a–14c. There are noticeable overlaps among the features that rank high with these methods, though the actual sequence of latent variables, understandably, show some differences. We show the actual distributions of some of these latent space embeddings in Figures 14d–14g. Generative models like VAEs trained on the popular celebrity protrait dataset CelebA [79] have successfully demonstrated disentanglement of semantics like age, gender, skin tone, hairstyle etc. [75] in latent space representation. In the context of the top tagging dataset, it is the jet kinematics that is embedded in the latent space. As seen from the NAP diagram in Figure 13b and the latent space feature distributions in Figures 14d–14g, the PFN latent space does not provide any disentanglement between the jet classes. In fact, for models like PFN that are trained to learn the jet classes and not the distribution of training dataset, the model has no additional incentive in disentangling the jet classes. Rather, PFN learns to embed the information regarding jet classes in correlations among latent features. This can be seen from the latent space correlation matrices of the two jet classes shown in Figure 15. The pairwise feature correlations are very different for the two jet classes, creating a clearer context for the classifier network  $F$  to obtain the desired jet classification.

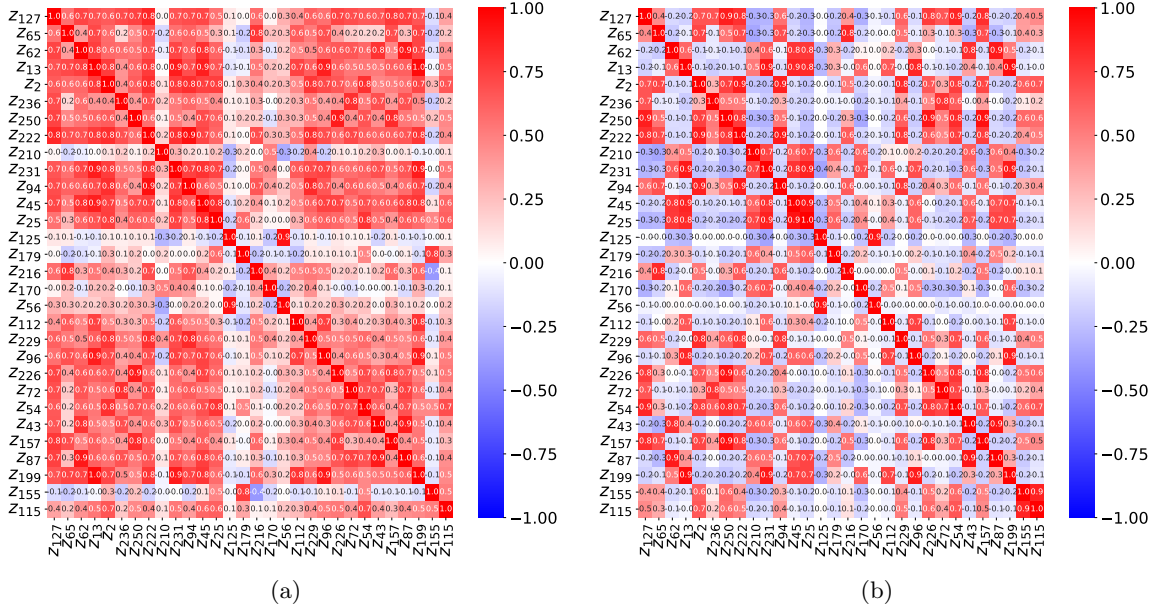


**Figure 15.** Correlation matrices for latent space features for (a) background QCD and (b) signal top jets. Only the top 30 latent features obtained from the  $\Delta\text{AUC}$  metric are shown.

We can further illustrate this by taking a deeper look into the correlations among the latent features. Since the size of the latent space is large but sparse, we select the top-ranking subset of latent features so that simultaneously masking each latent feature in the remaining subset causes at most 1% drop in the AUC score from the test data. For our baseline PFN model, this requires choosing 85 of the 256 latent features. One of

the classical data analysis tools to identify how features contribute to variability in data is Principal Component Analysis (PCA) [80]. PCA performs a linear transformation on these features to obtain a set of orthogonal feature spaces with no cross-correlation among the transformed features. The reduced feature space preserves the sample variance of the dataset but redistributes them along orthogonal basis vectors. We found that 99% of the sample variance of the test data was described by the top 30 principal components. We show the distribution of some of these components in Figures 16a- 16d. We can readily see how these PCA-transformed latent features can visibly differentiate between the two jet classes in Figures 16e- 16f.

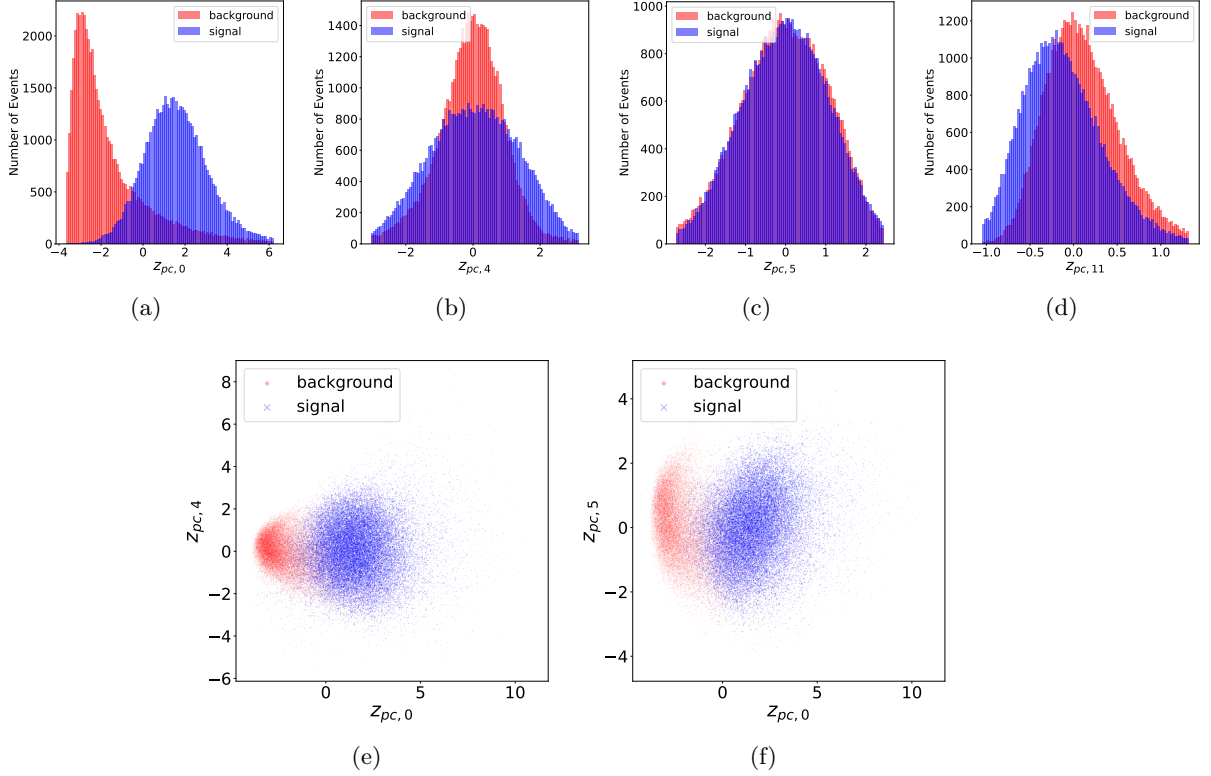


**Figure 16.** Distribution of some of the principal components for background QCD and signal top jets (top row) and pairwise distribution between these components for these jet classes (bottom row)

Strong disentanglement between the jet classes by the principal components of the latent space demonstrates how the jet class information is actually embedded in the correlation among different dimensions of the latent space. It is also instructive to investigate the physical nature of the latent space learned by the network. While it is neither trivial nor obvious for neural networks to learn about features that bear resemblance with features that bear meaning to humans, it has been seen that latent space networks can occasionally learn about physical variables [29]. In case of the PFN, since the latent space dimensions are highly correlated with each other, we chose to study the correlation between the principal components and jet features like jet mass, the number of constituents, and the subjettiness



variables which, as shown in Figures 1 and 2, can have moderate to strong discriminative feature. We found that the first principal component,  $z_{pc,0}$  (Figure 16a) shows a strong correlation with jet mass for both jet categories with correlation coefficients being 0.91 and 0.62 for background and signal jets respectively. This is particularly impressive considering that the network was trained with only information regarding the 3-momentum of the constituents and information about the energy or jet mass was absent from the set of inputs.  $z_{pc,0}$  also shows strong correlations with the number of jet constituents, while  $z_{pc,5}$ ,  $z_{pc,11}$  also appears to demonstrate moderate correlations with constituent multiplicity. None of the principal components showed strong correlations with the subjettiness variables and their ratios, implying the PFN model does not successfully reconstruct distributions similar to these variables.

## 5 Interpretability Inspires: The Augmented PFN Model

Our investigations into the explainability of multiple top tagger implementations in the previous section have led to a number of observations that can allow us to improve their performance.

- The PFN network shows a noticeable improvement in performance by allowing physics-inspired preprocessing to the inputs, originally prescribed in Ref. [24].
- It learns to moderately mimic the distribution of physical observables like jet mass and number of jet constituents in its latent space representations.
- The PFN latent space shows no significant correlations with the subjettiness variables that drive the top tagging performance of the MB8S network.
- The subjettiness variables  $\tau_x^{(0.5)}$  and  $\tau_x^{(2)}$  are highly correlated with the corresponding  $\tau_x^{(1)}$  variables, and their contribution to top tagging performance is marginal.

We can immediately infer from these observations that despite its spectacular performance, the PFN network fails to take advantage of the expressive properties of the subjettiness variables, leaving room for its improvement. Hence, we modify the PFN network to propose the Augmented PFN (AugPFN) model, defined as-

$$\text{AugPFN} = F \left( \sum_{i=0}^{N-1} \Phi(p_i) \cup \{\tau_x^{(1)}\}_{x=1}^7 \right) \quad (5.1)$$

Essentially, the underlying architecture of the AugPFN model is the same as that of PFN. The input to the  $F$  network is augmented with additional inputs, the  $\tau_x^{(1)}$  subjettiness variables. Taking inspiration from the NAP diagrams of the PFN model, we implement the  $\Phi$  network with three hidden layers of (100, 100, 64) nodes respectively. The  $F$  network, similarly, consists of two hidden layers each with 64 nodes. The particle-level momenta are preprocessed in the same way as for the PFN model and other hyperparameters of the model are also kept the same. Training the AugPFN network shows remarkable improvement over the PFN model. As shown in Table 2, AugPFN outperforms existing models by a large margin.

Model	Params	AUC	Acc	$1/\epsilon_B$
PELICAN [31]	45k	0.9869	0.9425	2289
LorentzNet [30]	220k	0.9868	0.9420	2195
ParticleNet [25, 33]	498k	0.9858	0.9400	1615
ParT [32]	2.14M	0.9877	0.944	2766
IN [29]	149k	0.9807	0.9300	775
PFN (baseline)	82k	0.9974	0.9772	8779
<b>AugPFN</b>	<b>26k</b>	<b>0.9999</b>	<b>0.9994</b>	<b>26152</b>

**Table 2.** Comparison of the performance of the PFN and AugPFN models compared to other architectures. The background rejection rate  $1/\epsilon_B$  is evaluated at a signal efficiency of 30%. The benchmark performance results of other models have been quoted from the corresponding references.

## 6 Conclusion

This paper presents a comprehensive study of the interpretability of DNN based top tagger models. Our work has unveiled a number of important aspects regarding how these models connect with the corresponding datasets. We have observed intriguing inconsistencies in feature ranking from different ranking methods, especially how the LRP method can produce a relevance distribution that can lead to a misleading interpretation of feature importance. Modifying LRP to obtain *differential* relevance scores has been found to be more consistent with other approaches in XAI. Furthermore, explainability metrics need to be carefully studied and understood for models trained with highly correlated input features since, as we show with the MB8S model, interpretability of AI models can be obscured in such cases. Our investigation suggests that models learn to embed jet class information in correlations among latent space embeddings and can learn to mimic distributions that closely resemble physical jet features. On the other hand, RNA scores and NAP diagrams can lead to an effective understanding of how information is propagated through different layers of a network and can lead to efficient model reoptimization strategies. This opens a possibility of incorporating these methods to obtain *in-situ* model optimization during training.

As this work shows, understanding how a model works can provide valuable insights into what a model learns and how it can be improved. While our work has rediscovered the potential of the PFN model by correctly implementing the prescribed preprocessing, thoroughly investigating its latent space distributions allowed us to discover its failure to take into account the expressive subjettness features. As a result, the proposed AugPFN model has learned to largely outperform rather novel deep learning architectures by simply augmenting the PFN latent space with the subjettness variables. Building on the tools and methods we have discussed in this work, our future work will take a deeper look into interpreting novel architectures like GNNs and transformers in the context of top tagging and more general jet classification scenarios.

## Acknowledgements

We would like to thank Volodymyr Kindratenko and the Center for Artificial Intelligence Innovation at the NCSA for support through our affiliation. This research is part of the Delta research computing project, which is supported by the National Science Foundation (award OCI 2005572), and the State of Illinois. Delta is a joint effort of the University of Illinois at Urbana-Champaign and its National Center for Supercomputing Applications. This work utilizes resources supported by the National Science Foundation’s Major Research Instrumentation program, grant 1725729, as well as the University of Illinois at Urbana-Champaign. We are grateful to Gregor Kasieczka and Huilin Qu for pointing us to important resources and code repositories. This work was supported by the FAIR Data program of the U.S. Department of Energy, Office of Science, Advanced Scientific Computing Research, under contract number DE-SC0021258 and by the U.S. Department of Energy, Office of Science, High Energy Physics, under contract number DE-SC0023365.

## A Performance of Baseline and variant models

Architecture	Description	Params	AUC	Acc	$1/\epsilon_B$	Sparsity
TopoDNN	<i>Baseline</i>	59k	0.971	0.916	278	0.705
	Trained without $p_{T,0}$	59k	0.970	0.914	267	0.852
	Hidden Layers: (240, 80, 10)	42k	0.972	0.916	309	0.818
	Hidden Layers: (120, 40, 6)	16k	0.972	0.916	305	0.584
MB8S	<i>Baseline</i>	57k	0.980	0.928	796	0.426
	Trained without jet $p_T$	57k	0.980	0.928	775	0.444
	Trained with $\{\tau_x^{(1)}\} \cup \{p_{T,J}, m_J\}$	55k	0.976	0.921	516	0.404
	Hidden Layers: (200, 200, 50)	55k	0.980	0.928	816	0.416
	Hidden Layers: (200, 200)	45k	0.980	0.928	775	0.452
PFN	<i>Baseline</i>	82k	0.997	0.977	8779	0.708 ( $\Phi$ ), 0.467 ( $F$ )
	$\Phi : (100, 100, 128)$	57k	0.997	0.976	33652	0.628 ( $\Phi$ ), 0.463 ( $F$ )
	$\Phi : (100, 100, 64)$	45k	0.994	0.971	1697	0.633 ( $\Phi$ ), 0.480 ( $F$ )
	$\Phi : (100, 100, 64), F : (64, 64)$	25k	0.995	0.972	2060	0.576 ( $\Phi$ ), 0.367 ( $F$ )
	$\Phi : (100, 64, 64), F : (64, 32)$	17k	0.995	0.969	1374	0.535 ( $\Phi$ ), 0.542 ( $F$ )

**Table A1.** Performance and sparsity of the baseline and model variants for different model architectures. The background rejection rate  $1/\epsilon_B$  is evaluated at a signal efficiency of 30%.

## References

- [1] T. Miller, Explanation in artificial intelligence: Insights from the social sciences, [Artificial Intelligence](#) **267** (2019) 1.
- [2] D. Gunning, M. Stefik, J. Choi, T. Miller, S. Stumpf and G.-Z. Yang, XAI—explainable artificial intelligence, [Science Robotics](#) **4** (2019) eaay7120.
- [3] P. Linardatos, V. Papastefanopoulos and S. Kotsiantis, Explainable AI: a review of machine learning interpretability methods, [Entropy](#) **23** (2020) 18.
- [4] G. Vilone and L. Longo, Explainable artificial intelligence: a systematic review, [arXiv preprint arXiv:2006.00093](#) (2020) .

- [5] M. Sahakyan, Z. Aung and T. Rahwan, Explainable artificial intelligence for tabular data: A survey, [\*IEEE Access\* \*\*9\*\* \(2021\) 135392](#).
- [6] H. Yuan, H. Yu, S. Gui and S. Ji, Explainability in graph neural networks: A taxonomic survey, [\*IEEE Transactions on Pattern Analysis and Machine Intelligence\* \(2022\)](#) .
- [7] D. Turvill, L. Barnby, B. Yuan and A. Zahir, A survey of interpretability of machine learning in accelerator-based high energy physics, in [2020 IEEE/ACM International Conference on Big Data Computing, Applications and Technologies \(BDCAT\)](#), pp. 77–86, 2020, [DOI](#).
- [8] Y.S. Lai, D. Neill, M. Płoskoń and F. Ringer, Explainable machine learning of the underlying physics of high-energy particle collisions, [\*Physics Letters B\* \*\*829\*\* \(2022\) 137055](#).
- [9] F. Mokhtar, R. Kansal, D. Diaz, J. Duarte, J. Pata, M. Pierini et al., Explaining machine-learned particle-flow reconstruction, [arXiv preprint arXiv:2111.12840](#) (2021) .
- [10] D.E. Kaplan, K. Rehermann, M.D. Schwartz and B. Tweedie, Top tagging: A method for identifying boosted hadronically decaying top quarks, [\*Phys. Rev. Lett.\* \*\*101\*\* \(2008\) 142001](#).
- [11] L.G. Almeida, S.J. Lee, G. Perez, I. Sung and J. Virzi, Top quark jets at the LHC, [\*Phys. Rev. D\* \*\*79\*\* \(2009\) 074012](#).
- [12] L.G. Almeida, S.J. Lee, G. Perez, G. Sterman and I. Sung, Template overlap method for massive jets, [\*Physical Review D\* \*\*82\*\* \(2010\) 054034](#).
- [13] T. Plehn and M. Spannowsky, Top tagging, [\*Journal of Physics G: Nuclear and Particle Physics\* \*\*39\*\* \(2012\) 083001](#).
- [14] The ATLAS Collaboration, Identification of high transverse momentum top quarks in pp collisions at  $\sqrt{s} = 8$  tev with the ATLAS detector, [\*Journal of high energy physics\* \*\*2016\*\* \(2016\) 1](#).
- [15] The CMS Collaboration, A Cambridge-Aachen (C-A) based Jet Algorithm for boosted top-jet tagging, Tech. Rep. [CMS-PAS-JME-09-001](#), CERN, Geneva (2009).
- [16] The CMS Collaboration, Boosted Top Jet Tagging at CMS, Tech. Rep. [CMS-PAS-JME-13-007](#), CERN, Geneva (2014).
- [17] The ATLAS Collaboration, Performance of top-quark and  $w$ -boson tagging with atlas in run 2 of the lh, [\*Eur. Phys. J. C\* \*\*79\*\* \(2019\) 1](#).
- [18] CMS collaboration, Identification of heavy, energetic, hadronically decaying particles using machine-learning techniques, [\*Journal of Instrumentation\* \(2020\)](#) .
- [19] J. Pearkes, W. Fedorko, A. Lister and C. Gay, Jet constituents for deep neural network based top quark tagging, [arXiv preprint arXiv:1704.02124](#) (2017) .
- [20] L. Moore, K. Nordström, S. Varma and M. Fairbairn, Reports of my demise are greatly exaggerated:  $N$ -subjettiness taggers take on jet images, [\*SciPost Phys.\* \*\*7\*\* \(2019\) 036](#).
- [21] K. Datta and A. Larkoski, How much information is in a jet?, [\*J. High Energy Phys.\* \*\*2017\*\* \(2017\) 1](#).
- [22] G. Louppe, K. Cho, C. Becot and K. Cranmer, QCD-aware recursive neural networks for jet physics, [\*Journal of High Energy Physics\* \*\*2019\*\* \(2019\) 1](#).
- [23] A. Butter, G. Kasieczka, T. Plehn and M. Russell, Deep-learned top tagging with a Lorentz layer, [\*SciPost Physics\* \*\*5\*\* \(2018\) 028](#).

- [24] P.T. Komiske, E.M. Metodiev and J. Thaler, Energy flow networks: deep sets for particle jets, *Journal of High Energy Physics* **2019** (2019) 1.
- [25] H. Qu and L. Gouskos, Jet tagging via particle clouds, *Physical Review D* **101** (2020) .
- [26] S. Macaluso and D. Shih, Pulling out all the tops with computer vision and deep learning, *Journal of High Energy Physics* **2018** (2018) 1.
- [27] M. Erdmann, E. Geiser, Y. Rath and M. Rieger, Lorentz boost networks: autonomous physics-inspired feature engineering, *Journal of Instrumentation* **14** (2019) P06006.
- [28] S. Egan, W. Fedorko, A. Lister, J. Pearkes and C. Gay, Long short-term memory (LSTM) networks with jet constituents for boosted top tagging at the lhc, *arXiv preprint arXiv:1711.09059* (2017) .
- [29] E.A. Moreno, O. Cerri, J.M. Duarte, H.B. Newman, T.Q. Nguyen, A. Periwai et al., JEDI-net: a jet identification algorithm based on interaction networks, *The European Physical Journal C* **80** (2020) 1.
- [30] S. Gong, Q. Meng, J. Zhang, H. Qu, C. Li, S. Qian et al., An efficient lorentz equivariant graph neural network for jet tagging, *arXiv preprint arXiv:2201.08187* (2022) .
- [31] A. Bogatskiy, T. Hoffman, D.W. Miller and J.T. Offermann, Pelican: Permutation equivariant and lorentz invariant or covariant aggregator network for particle physics, *arXiv preprint arXiv:2211.00454* (2022) .
- [32] H. Qu, C. Li and S. Qian, Particle transformer for jet tagging, *arXiv preprint arXiv:2202.03772* (2022) .
- [33] G. Kasieczka, T. Plehn, A. Butter, K. Cranmer, D. Debnath, B.M. Dillon et al., The machine learning landscape of top taggers, *SciPost Physics* **7** (2019) 14.
- [34] K. Hornik, M. Stinchcombe and H. White, Multilayer feedforward networks are universal approximators, *Neural networks* **2** (1989) 359.
- [35] A. Chakraborty, S.H. Lim and M.M. Nojiri, Interpretable deep learning for two-prong jet classification with jet spectra, *Journal of High Energy Physics* **2019** (2019) 1.
- [36] G. Agarwal, L. Hay, I. Iashvili, B. Mannix, C. McLean, M. Morris et al., Explainable AI for ML jet taggers using expert variables and layerwise relevance propagation, *Journal of High Energy Physics* **2021** (2021) 1.
- [37] P. Shanahan, K. Terao and D. Whiteson, Snowmass 2021 computational frontier CompF03 topical group report: Machine learning, *arXiv preprint arXiv:2209.07559* (2022) .
- [38] D. Seuß, Bridging the gap between explainable AI and uncertainty quantification to enhance trustability, *arXiv preprint arXiv:2105.11828* (2021) .
- [39] C. Grojean, A. Paul, Z. Qian and I. Strümke, Lessons on interpretable machine learning from particle physics, *Nature Reviews Physics* (2022) 1.
- [40] J. Duarte, S. Han, P. Harris, S. Jindariani, E. Kreinar, B. Kreis et al., Fast inference of deep neural networks in FPGAs for particle physics, *Journal of Instrumentation* **13** (2018) P07027.
- [41] Y. Iiyama, G. Cerminara, A. Gupta, J. Kieseler, V. Loncar, M. Pierini et al., Distance-weighted graph neural networks on fpgas for real-time particle reconstruction in high energy physics, *Frontiers in big Data* (2021) 44.

- [42] A. Heintz, V. Razavimaleki, J. Duarte, G. DeZoort, I. Ojalvo, S. Thais et al., Accelerated charged particle tracking with graph neural networks on FPGAs, arXiv preprint arXiv:2012.01563 (2020) .
- [43] A. Roy and M.S. Neubauer, “Interpretability of an interaction network for identifying  $h \rightarrow b\bar{b}$  jets”, <https://agenda.infn.it/event/28874/contributions/169216/>.”
- [44] M.S. Neubauer and A. Roy, Explainable AI for high energy physics, arXiv preprint arXiv:2206.06632. Contribution to Snowmass 2021 (2022) .
- [45] E.A. Moreno, T.Q. Nguyen, J.-R. Vlimant, O. Cerri, H.B. Newman, A. Periwai et al., Interaction networks for the identification of boosted  $h \rightarrow b\bar{b}$  decays, Physical Review D **102** (2020) 012010.
- [46] “Top tagging dataset, available at: <https://desycloud.desy.de/index.php/s/llbX3zpLhazgPJ6>.”
- [47] T. Sjöstrand, S. Ask, J.R. Christiansen, R. Corke, N. Desai, P. Ilten et al., An introduction to PYTHIA 8.2, Computer Physics Communications **191** (2015) 159.
- [48] J. De Favereau, C. Delaere, P. Demin, A. Giammanco, V. Lemaitre, A. Mertens et al., DELPHES 3: a modular framework for fast simulation of a generic collider experiment, Journal of High Energy Physics **2014** (2014) 1.
- [49] M. Cacciari, G.P. Salam and G. Soyez, The anti- $k_t$  jet clustering algorithm, Journal of High Energy Physics **2008** (2008) 063.
- [50] M. Cacciari, G.P. Salam and G. Soyez, FastJet user manual, The European Physical Journal C **72** (2012) 1.
- [51] J. Thaler and K. Van Tilburg, Identifying boosted objects with N-subjettiness, Journal of High Energy Physics **2011** (2011) 1.
- [52] S.D. Ellis and D.E. Soper, Successive combination jet algorithm for hadron collisions, Physical Review D **48** (1993) 3160.
- [53] G.C. Blazeya, J.R. Dittmannb, S.D. Ellisc, V.D. Elvirab, K. Framed, S. Grinstein et al., Run II jet physics, QCD and Weak Boson Physics in Run II (2000) 47.
- [54] M. Zaheer, S. Kottur, S. Ravanbakhsh, B. Póczos, R. Salakhutdinov and A.J. Smola, Deep sets, in Proceedings of the 31st International Conference on Neural Information Processing Systems, pp. 3394–3404, 2017.
- [55] R. Wang and K. Tang, Feature selection for maximizing the area under the ROC curve, in 2009 IEEE International Conference on Data Mining Workshops, pp. 400–405, IEEE, 2009.
- [56] J. van der Waa, E. Nieuwburg, A. Cremers and M. Neerincx, Evaluating XAI: A comparison of rule-based and example-based explanations, Artificial Intelligence **291** (2021) 103404.
- [57] S. Jesus, C. Belém, V. Balayan, J. Bento, P. Saleiro, P. Bizarro et al., How can I choose an explainer? an application-grounded evaluation of post-hoc explanations, in Proceedings of the 2021 ACM Conference on Fairness, Accountability, and Transparency, pp. 805–815, 2021.
- [58] J. Tang, S. Alelyani and H. Liu, Feature selection for classification: A review, Data classification: Algorithms and applications (2014) 37.
- [59] M.T. Ribeiro, S. Singh and C. Guestrin, Why should I trust you? explaining the predictions of any classifier, in Proceedings of the 22nd ACM SIGKDD international conference on knowledge discovery and data mining, pp. 1135–1144, 2016.

- [60] X.-w. Chen and M. Wasikowski, Fast: a ROC-based feature selection metric for small samples and imbalanced data classification problems, in Proceedings of the 14th ACM SIGKDD international conference on Knowledge discovery and data mining, pp. 124–132, 2008.
- [61] A.J. Serrano, E. Soria, J.D. Martin, R. Magdalena and J. Gomez, Feature selection using ROC curves on classification problems, in The 2010 international joint conference on neural networks (IJCNN), pp. 1–6, IEEE, 2010.
- [62] S.M. Lundberg and S.-I. Lee, A unified approach to interpreting model predictions, Advances in Neural Information Processing Systems (NeurIPS) **30** (2017) .
- [63] M.T. Ribeiro, S. Singh and C. Guestrin, Model-agnostic interpretability of machine learning, arXiv preprint arXiv:1606.05386 (2016) .
- [64] A. Binder, S. Bach, G. Montavon, K.-R. Müller and W. Samek, Layer-wise relevance propagation for deep neural network architectures, in Information science and applications (ICISA) 2016, pp. 913–922, Springer (2016).
- [65] G. Montavon, A. Binder, S. Lapuschkin, W. Samek and K.-R. Müller, Layer-wise relevance propagation: an overview, Explainable AI: interpreting, explaining and visualizing deep learning (2019) 193.
- [66] S. Bach, A. Binder, G. Montavon, F. Klauschen, K.-R. Müller and W. Samek, On pixel-wise explanations for non-linear classifier decisions by layer-wise relevance propagation, PloS one **10** (2015) e0130140.
- [67] T. Schnake, O. Eberle, J. Lederer, S. Nakajima, K.T. Schutt, K.-R. Mueller et al., Higher-order explanations of graph neural networks via relevant walks, IEEE Transactions on Pattern Analysis & Machine Intelligence (2021) 1.
- [68] L. Toloşi and T. Lengauer, Classification with correlated features: unreliability of feature ranking and solutions, Bioinformatics **27** (2011) 1986.
- [69] G. Montavon, S. Lapuschkin, A. Binder, W. Samek and K.-R. Müller, Explaining nonlinear classification decisions with deep taylor decomposition, Pattern recognition **65** (2017) 211.
- [70] B.O. Ayinde, T. Inanc and J.M. Zurada, Regularizing deep neural networks by enhancing diversity in feature extraction, IEEE transactions on neural networks and learning systems **30** (2019) 2650.
- [71] M. Cogswell, F. Ahmed, R. Girshick, L. Zitnick and D. Batra, Reducing overfitting in deep networks by decorrelating representations, arXiv preprint arXiv:1511.06068 (2015) .
- [72] H. Kaur, H. Nori, S. Jenkins, R. Caruana, H. Wallach and J. Wortman Vaughan, Interpreting interpretability: understanding data scientists’ use of interpretability tools for machine learning, in Proceedings of the 2020 CHI conference on human factors in computing systems, pp. 1–14, 2020.
- [73] N. Srivastava, G. Hinton, A. Krizhevsky, I. Sutskever and R. Salakhutdinov, Dropout: a simple way to prevent neural networks from overfitting, The journal of machine learning research **15** (2014) 1929.
- [74] D.P. Kingma and M. Welling, Auto-encoding variational Bayes, arXiv preprint arXiv:1312.6114 (2013) .
- [75] C.P. Burgess, I. Higgins, A. Pal, L. Matthey, N. Watters, G. Desjardins et al., Understanding disentangling in  $\beta$ -VAE, arXiv preprint arXiv:1804.03599 (2018) .



- [76] G. Hadjeres, F. Nielsen and F. Pachet, GLSR-VAE: Geodesic latent space regularization for variational autoencoder architectures, in 2017 IEEE Symposium Series on Computational Intelligence (SSCI), pp. 1–7, IEEE, 2017.
- [77] C. Bajaj, A. Roy and H. Zhang, Invariance-based multi-clustering of latent space embeddings for equivariant learning, arXiv preprint [arXiv:2107.11717](https://arxiv.org/abs/2107.11717) (2021) .
- [78] B. Bortolato, A. Smolkovič, B.M. Dillon and J.F. Kamenik, Bump hunting in latent space, Physical Review D **105** (2022) 115009.
- [79] Z. Liu, P. Luo, X. Wang and X. Tang, Deep learning face attributes in the wild, in Proceedings of International Conference on Computer Vision (ICCV), December, 2015.
- [80] I.T. Jolliffe and J. Cadima, Principal component analysis: a review and recent developments, Philosophical Transactions of the Royal Society A: Mathematical, Physical and Engineering Sciences **374** (2016) 20150202.